A Fast Approach for In Situ SoC Estimation of a Hybrid Supercapacitor Based on GPR and EIS Measurements

A Fast Approach for In Situ SoC Estimation of a Hybrid Supercapacitor Based on GPR and EIS Measurements

Gabriele Patrizi, *Member, IEEE*, Sadia Ali, *Member, IEEE*, Lorenzo Ciani, *Senior Member, IEEE*, Fabio Canzanella, *Member, IEEE*, Ilaria De Munari, *Senior Member, IEEE*, and Valentina Bianchi, *Senior Member, IEEE*

***Abstract*—A fast and accurate approach for the state-of-charge (SoC) estimation of a hybrid supercapacitor (HSC) is presented in this article. Electrochemical impedance spectroscopy (EIS) is performed with the HSC as the device under test (DUT). The EIS is initially performed at six different frequencies (0.05, 0.1, 0.5, 1, 5, and 10 Hz), collecting a dataset, including 6000 points describing SoC in the range from 100% to 0%. This collected dataset is then utilized for extensive training and testing of a Gaussian process regression (GPR) model with a nonisotropic exponential kernel and Bayesian optimization to accurately estimate the SoC of the HSC. To simplify the measurement setup and procedure, aiming at developing an in situ instrument for SoC evaluation, in the recognition process, a limited number of frequencies should be used. Moreover, special attention should be paid to the measurement time, leading to preferring higher frequencies over the lower ones. For this reason, a combination of only two frequency points (FPs) has been identified, for the best compromise between accuracy and timing, also considering the typical discharge curve of the HSC, which presents an abrupt decrease at low values of SoC. Data acquired at 0.1 Hz have been used to train the GPR model for SoC values within the range [30, 100], while the data acquired at 1 Hz have been exploited for SoC values within the range [0, 30]. Later, a postprocessing phase is applied, including a three-point linearization and an error calibration, which further improves the estimation accuracy. The resulting average root-mean-squared error (RMSE) for the proposed approach without and with the postprocessing phase came out to be 1.33 and 0.94, respectively, which are very good results compared with more complex approaches in the literature.**

***Index Terms*—Electrochemical impedance spectroscopy (EIS), frequency-selective approach, Gaussian process regression (GPR), machine learning (ML), state-of-charge (SoC) , supercapacitor (SC).**

I. INTRODUCTION

ENERGY storage systems (ESSs) are currently widespread in many application areas [1]. The use of ESS requires a complex management device for cell balancing, temperature monitoring, and the estimation of state-of-charge (SoC) and state-of-health (SoH) [2]. The SoC estimation is currently a prominent research area in the field of electric vehicles (EVs) since an accurate prediction elevates the consumer's confidence in EVs [3].

The ESS encompasses multiple technologies such as lithium-ion battery (LiB), solid-state batteries, ammonia-based storage, and supercapacitors (SCs). In contrast to the other technologies, the SCs exhibit superior power density, better overall efficiency, and are also more suitable for compact applications [4]. Moreover, the SCs tend to have a larger operating cycle duration [5] and a wider operating temperature range, gaining popularity as a stand-alone device or as part of a hybrid ESS setup [6]. The broader term SC encompasses three subtypes, i.e., symmetric double-layer capacitors, battery capacitors based on pseudo-capacitance, and hybrid SCs (HSCs) [7]. An HSC combines the features of an SC and a battery to improve the overall performance [8].

A detailed review of SoC estimation techniques in [8] compares direct methods, i.e., coulomb counting (CC), open-circuit voltage (OCV), and impedance measurement-based estimation, with indirect methods, i.e., electrical circuit model, adaptive filters, and artificial intelligence (AI)-based techniques. The latter stands out particularly due to their improved learning capabilities, greater efficiency, and convergence [9]. For this reason, multiple machine learning (ML)-based algorithms are available for the accurate estimation of the SoC in an ESS [10]. Plenty of research has been done in this regard with different ESSs and using different techniques. In [11], a Gaussian process regression (GPR) model and a long short-term memory (LSTM) neural network (NN) are paired up, alongside an error correction algorithm for the LiB, achieving an average root-mean-squared error (RMSE) of 0.382%. A deep feedforward NN is presented in [12] for direct mapping of the input features onto the SoC. The resulting mean absolute error (MAE) is 1.10% and 2.17% in the case of an operating temperature of 25 °C and −20 °C, respectively. The ML technique utilized in [13] incorporates a convolutional NN (CNN) alongside some preprocessing steps (i.e., median filtering and feature extraction), resulting in an RMSE of less than 3.71%.

Among other ML-based regression techniques, the GPR stands out for its flexibility and its ability to quantify uncertainty [14]. A multibattery analysis incorporating GPR and

Received 23 October 2025; revised 14 January 2026; accepted 28 January 2026. Date of publication 23 February 2026; date of current version 5 March 2026. The Associate Editor coordinating the review process was Dr. Helko E. van den Brom. *(Corresponding author: Lorenzo Ciani.)*

Gabriele Patrizi, Lorenzo Ciani, and Fabio Canzanella are with the Department of Information Engineering, University of Florence, 50139 Florence, Italy (e-mail: lorenzo.ciani@unifi.it).

Sadia Ali is with the Department of Engineering and Architecture, University of Parma, 43121 Parma, Italy, and also with the University of Bologna, 40126 Bologna, Italy.

Ilaria De Munari and Valentina Bianchi are with the Department of Engineering and Architecture, University of Parma, 43121 Parma, Italy.

Digital Object Identifier 10.1109/TIM.2026.3667312

an adaptive approach is conducted in [15]. The training data are collected from three different batteries (lithium-ion, nickel metal hydride, and lithium polymer), and a GPR with a radial bias function (RBF) kernel obtained similar RMSE for the different technologies. A gated recurrent unit (GRU)-based deep recurrent kernel alongside GPR is introduced in [16], with final average MAE over three temperature setpoints (0 °C, 10 °C, and 25 °C) reported at 0.79%. The performance superiority of the GPR as opposed to other ML algorithms, such as support vector machine (SVM) and linear regression, has also been validated in [17], achieving RMSE considerably less than that of SVM and linear regression, analyzing two different datasets.

As with any ML algorithm, the estimation capabilities depend largely on the length of the dataset, the number of features, and their nature [18]. Within the standard arrangement, the voltage, current, and temperature of the ESS are usually designated as the training features when it comes to the estimation of the SoC [19]. However, with the uncertain aging process within the ESS, sometimes these traditional features fail to fully capture the internal dynamics of the system under study, resulting in a subpar estimation [20]. A rather interesting technology, known as electrochemical impedance spectroscopy (EIS), primarily used to measure the internal impedance of the ESSs at different frequencies, can be utilized for accurate SoC estimation [21]. Given that the EIS technique can compute the internal impedance, which can model the aging of the battery in a more dynamic manner, this technique is a viable candidate to be used alongside an ML algorithm for the accurate SoC estimation of an ESS. In [22], a classification-based ML model in conjunction with an electric circuit-based model (ECM) is deployed for accurate SoC estimation of LiB cells based on EIS measurements at 14 different logarithmically spaced frequencies. Another EIS-based SoC estimation for LiB is reported in [23] using a deep NN (DNN) trained with EIS measurements taken at 25 different frequencies, reaching RMSE of 3.80% in the SoC range from 30% to 95%. A CNN combined with a random forest (RF) trained on the parameters from EIS is presented in [24], analyzing the battery pack of an EV.

The EIS technique can provide multiple features that are utilized during the training phase of the ML-based algorithm. The most common features include the modulus, phase, real, and imaginary parts of the impedance of the ESS [25].

The SoC of an ESS, such as the LiB, has been extensively investigated and monitored in the existing literature [26]. On the other hand, the SC presents a wider research gap [27]. A Kalman filter and a fractional order model are used in [28] for SoC estimation of a traditional SC under various operating conditions, achieving a percentage error under 1.3%. Instead, [29] presents a model parameter identification phase for SCs followed by an OCV analysis based on a Kalman filter. An unscented Kalman filter algorithm related to a fractional order model is presented in [30] for traditional SCs tested under different temperature conditions, resulting in a maximum RMSE of less than 1.8%. Overall, the above citations suffer from a number of drawbacks, such as a limited SoC range, intricate ML algorithms that present a more complex architecture, and added complications pertaining to the inclusion of model-based techniques such as ECM. Moreover, generally, too many frequencies are included during the EIS procedure, which further complicates the measurement procedure and increases the measurement time.

The research presented in this article is an extension of [31], where a single-frequency (100 mHz) EIS measurement on an HSC is used by a GPR model, achieving an RMSE of 1.56%. The major contributions of this work are summarized as follows.

1) This article presents an unbiased and fast in situ approach to estimate the SoC of an HSC, which is a topic barely considered in the literature.
2) A dual-frequency EIS approach is presented, incorporating one lower and one considerably higher frequency as a compromise to reduce measurement time and maintain simplicity in the architecture.
3) The parameters measured during the EIS are processed to estimate the SoC, using a GPR-based regression technique with a nonisotropic kernel.
4) To further improve efficiency, a postprocessing algorithm is deployed, performing a three-point linearization, followed by error calibration.
5) The overall technique presents very good results in comparison to existing literature and provides a solid benchmark for future research in the collective field of SoC, HSC, and EIS.

The rest of this article is arranged as follows. Section II covers the details of the methods incorporated in the proposed framework. Section III presents the data acquisition phase. Section IV presents the analysis of the obtained results and quantitative comparison, followed by the conclusion in Section V.

II. Methods

A. State-of-Charge

The SoC of an ESS is commonly defined as the percentage of the remaining capacity of the ESS with respect to the rated capacity at a particular discharge rate. The mathematical representation is provided by the following equation:

$$SoC = \frac{Q_c}{Q_R} \times 100 \tag{1}$$

where Q_c represents the current capacity (i.e., releasable capacity) and Q_R represents the rated capacity of the ESS. A fully charged ESS corresponds to a 100% value, whereas a fully discharged one corresponds to 0% SoC.

B. Electrochemical Impedance Spectroscopy

The EIS is a nondestructive procedure specifically designed to understand the internal dynamics of an ESS and study its aging behavior through impedance measurement. The experiment is performed by applying small AC voltages at specific frequencies to the device under test (DUT) and recording the impedance parameters as output. This way, the response of the DUT is studied across a wide range of frequencies. The EIS has multiple application areas; it can be used to study the internal mechanisms of different elements of the cell, such as electrode materials, corrosion protection, solid electrolyte, and conductive polymer [25]. Moreover, EIS is able to deduce multiple physical properties such as pore distributions, electrolytic resistance of the pores, interfacial impedance, and charge-transfer resistance [32]. The ratio of the applied AC voltage signal and the resulting current provides the corresponding impedance of the ESS. The mathematical expression of the process is

$$Z\left(2\pi f_j\right) = \frac{E\left(t\right)}{I\left(t\right)} = \frac{\sum_{J=1}^{M} e_J \times \sin\left(2\pi f_J t\right)}{\sum_{J=1}^{M} i_J \times \sin\left(2\pi f_J t + \beta_J\right)} \tag{2}$$

where $Z(2\pi f_j)$ represents a complex quantity, i.e., impedance, describing the internal dynamics of the ESS. $E(t)$ represents the AC voltage perturbation. e_J stands for the amplitude. f_J is the frequency of each individual iteration. Instead, $I(t)$ represents the AC current responses, i_J stands for the amplitude, and β_J is the phase of each individual iteration. M represents the total number of frequency components considered during the EIS procedure.

C. Gaussian Process Regression

A Gaussian distribution refers to a bell-shaped probabilistic distribution that is symmetrically centered around its mean value μ, while the standard deviation σ quantifies the degree of uncertainty or dispersion within the data. The probability density function (pdf) of the Gaussian distribution for a random variable O is defined as follows:

$$PDF_O\left(z\right) \sim \mathcal{N}\left(\mu, \sigma^2\right) = \frac{1}{\sqrt{2\pi\sigma}} e^{-\frac{(z-\mu)^2}{2\sigma^2}} \tag{3}$$

where z denotes the continuous random variable, while $N(\mu, \sigma^2)$ is the Gaussian distribution. In regression-based modeling, the characterization of joint probability distribution is essential, as independent marginal distributions fail to capture the inherent correlations among closely related data points. Neglecting these dependencies can result in suboptimal regression performance since the core objective of regression analysis lies in modeling the interrelationship among feature variables [16]. ML algorithms typically incorporate multiple features to effectively describe system behavior; thus, in GPR, the multivariate Gaussian distribution is employed to jointly model these relationships. It is mathematically expressed as follows:

$$\mathcal{N}\left(z \,|\, \mu, k\right) = \frac{1}{(2\pi)^{\frac{D}{2}} \, |k|^{\frac{1}{2}}} e^{\left[-\frac{1}{2}(z-\mu)^T k^{-1}(z-\mu)\right]} \tag{4}$$

where D represents the data dimensionality, μ represents the mean vector, and k is the kernel function. A $D \times D$ covariance matrix that contains the pairwise covariances of all the jointly modeled random variables.

A GPR model, given its nonparametric nature, can take into consideration all the possible functions and can work with any sample set of these functions. In GPR, the probability distributions of all the functions are computed, with the mean value corresponding to the maximum likelihood estimate, and the variance providing a quantitative measure of uncertainty, serving as an indicator of predictive confidence. A GPR model can be implemented to demonstrate accurate predictive quality, considering the following joint probability distribution:

$$\begin{bmatrix} F \\ F^* \end{bmatrix} \sim N\left(\begin{bmatrix} \dfrac{m(Z)}{m(Z^*)} \end{bmatrix}, \begin{bmatrix} k\left(Z, Z\right) + \sigma_n^2 I & k\left(Z, Z^*\right) \\ k\left(Z^*, Z\right) & k\left(Z^*, Z^*\right) \end{bmatrix}\right) \tag{5}$$

where $Z = [z_1, z_2, \ldots, z_n]$ represents the training dataset; $Z^* = [z_1^*, z_2^*, \ldots, z_n^*]$ represents the test dataset; $k(\cdot, \cdot)$ represents the kernel function; $m(\cdot)$ represents the mean function; σ_n^2 represents the covariance; and $F = [F(z_1), F(z_2), \ldots, F(z_n)]$ and $F^* = [F^*(z_1), F^*(z_2), \ldots, F^{*I}(z_n)]$ represent the output function values for Z and Z^*, respectively.

The performance and generalization capability of a GPR model are highly dependent on the choice of kernel function. Distinct kernel functions can yield significantly different predictive behaviors, even when applied to the same dataset. In the proposed framework, the anisotropic exponential kernel was employed, combined with Bayesian optimization for hyperparameter tuning within the MATLAB/Simulink environment. Unlike the widely adopted squared exponential (SE) kernel, the anisotropic exponential kernel offers enhanced flexibility in capturing similarities, particularly for datasets with varying dimensional characteristics and heterogeneous scaling factors [33]. As the dimensionality of the training data increases, conventional kernels such as the RBF kernel may exhibit deteriorating convergence and reduced accuracy. In contrast, the scaling adaptability of the anisotropic exponential kernel enables superior predictive accuracy and generalization performance [34]. The kernel mathematical representation is given as follows:

$$k\left(Z, Z^* | \varphi\right) = \sigma_n^2 e^{\left[-\frac{1}{2} r^2\right]} \tag{6}$$

where $r = ((((z_n - z_n^*)^2)/\vartheta_n^2))^{1/2}$ represents the Euclidean distance between z_n and z_n^*, ϑ_n^2 represents the length scales, and $\varphi_n = \log\log\vartheta_n$ represents the unconstrained parametrization for n dimensions. The proposed GPR framework, incorporating the anisotropic exponential kernel, is thus employed in this work to achieve an accurate estimation of the SoC for the HSC system.

D. Postprocessing Phase

In order to obtain a reduced overall error and systematic noise, a postprocessing phase can be applied to the predicted SoC from the GPR model. In the proposed framework, the postprocessing strategy comprises two main stages applied to the outputs generated by the GPR model: linear interpolation and error calibration. The linear interpolation is implemented using a switching mechanism based on the Euclidean distance between the interpolated and the predicted values and a predefined threshold. Specifically, when the predicted value deviates significantly from the interpolated result, the model identifies this as an indication of poor prediction performance by the GPR and consequently substitutes the prediction with the interpolated value at that specific test point [31]. The interpolation parameters are computed as follows:

$$m = \frac{\left[F^*\left(n+1\right) - F^*\left(n-1\right)\right]}{2} \tag{7}$$

$$q = \frac{\left[F^*\left(n+1\right)\cdot\left(n-1\right) - F^*\left(n-1\right)\cdot\left(n+1\right)\right]}{2} \tag{8}$$

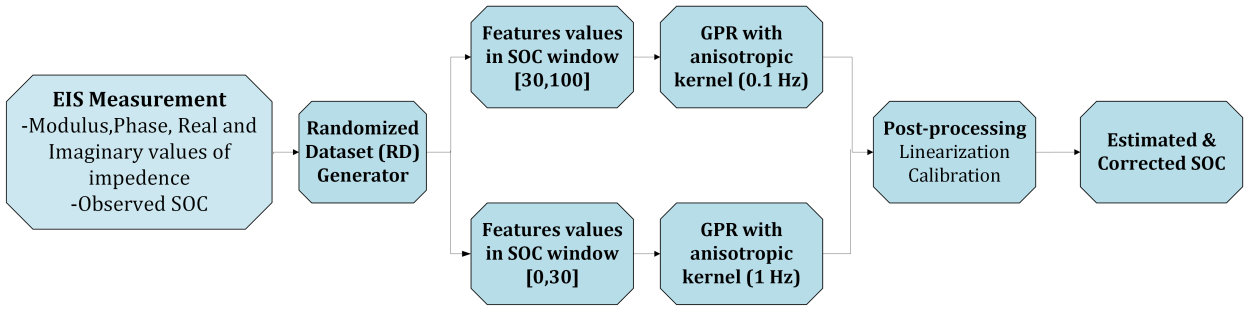

Fig. 1. Flowchart for the proposed framework (single iteration).

where m and q are the slope and intercept of the interpolation line, respectively; and F^* represents the values predicted by the GPR.

Following interpolation, an error calibration phase is introduced to further enhance the accuracy. This calibration compensates for the static nature and limited informational content in certain regions of the input feature space and specifically the modulus, phase, and the real and imaginary components of the HSC impedance [31]. The calibration process utilizes data from the first controlled discharge cycle to correct subsequent test cycles, thereby reducing the cumulative error in the estimated SoC [11]. The details of the proposed framework, in the form of a flowchart, are also summarized in Fig. 1. The figure represents the dynamics of a single iteration for the training and consequent testing of the GPR model.

III. Data Acquisition

A. Device Under Test

The device examined in this experimental procedure is a cylindrical battery-like HSC, referred to as a 4.2-V 4000-F rechargeable capacitor of nanopouch and developed by GongHe Electronics Company Ltd. [35]. More specifically, the DUT exhibits a nominal capacity of 4000 F and a maximum voltage of 4.2 V. The cell can sustain continuously up to 5 A in discharge and up to 10 A in pulse mode, while the suggested charge current is 2 A. The HSC can work in both operating conditions in a wide thermal range between −20 °C and 55 °C. As stated by the manufacturer, the nominal internal resistance is specified to be lower than 15 mΩ when measured under AC conditions at a frequency of 1 kHz.

B. Testing Procedure

The experimental campaign has the scope of collecting EIS data at different SoCs for selected frequency points (FPs) in the range between 50 mHz and 10 Hz. In detail, the testing procedure consists of 20 cycles, in which the cell is charged up to 100% SoC with a CCCV strategy at 2 A (i.e., 0.5C) with a voltage cutoff of 4.2 V and a current cutoff of 200 mA. After a rest time of 30 min to stabilize the cell, the HSC is discharged in steps of 2% of the SoC with a constant current of 2 A. The selected charge and discharge rates are recommended by the manufacturer as nonstressful operating conditions, allowing to minimize their impact on the HSCs and preventing accelerated aging. More specifically, different

TABLE I
Experimental Procedure

Workflow of the testing procedure	
Input:	*SoC* = State-of-Charge of the HSC *N* = Cycle index STEP = Step index
Start 1. Set Temperature = 20 °C 2. Set Humidity = 50% 3. **for** N = 1 **to** 20 **do** 4. Charge the HSC up to SoC = 100% 5. The cell rests for 30 minutes 6. EIS measurement at 100% SoC condition 7. **for** STEP = 1 **to** 50 **do** 8. **for** f = {0.05, 0.1, 0.5, 1, 5, 10} 9. discharge the cell until SoC = [100 – (2•STEP)] % 10. cell rests for 3 minutes 11. perform the EIS measurement at frequency f [Hz] 12. **end** 13. **end** 14. **end** 15. **End** test	
Output: dataset of EIS measurements at selected frequency points	

charge rates can induce varying degrees of cell polarization; however, these effects can be largely mitigated by introducing adequate rest periods [36]. On the other hand, varying the discharge rates not only increases the stress on the cell but also leads to larger voltage drops at each step, which would require longer stabilization times. Such extended pauses, however, are not compatible with the experimental requirements. For this reason, only nonstressful charge/discharge profiles have been considered.

At the end of each discharge step, after a 3-min rest phase, an EIS measurement is performed at six different frequency setpoints, namely, 50 mHz, 100 mHz, 500 mHz, 1 Hz, 5 Hz, and 10 Hz. The spectroscopy is conducted in a potentiostatic mode by applying a sinusoidal voltage signal of 1 mV without a DC offset. At the end of each sequence, the DC internal resistance is measured with 50-mA current pulses of duration 1 ms. The cycle ends when the 0% SoC condition is reached. All experimental conditions were carefully controlled to ensure the uniformity of data and test environments. Specifically, temperature and relative humidity were fixed at 20 °C and 50%, respectively, and maintained constant throughout all

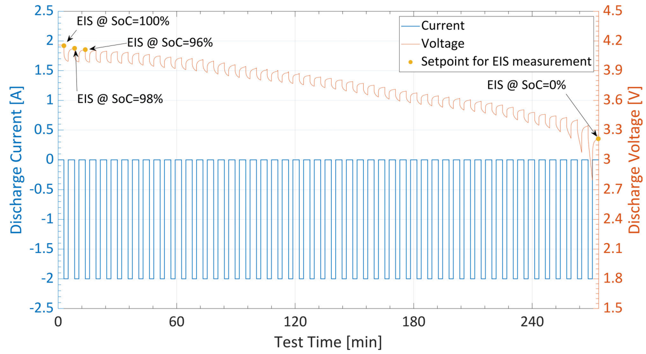

Fig. 2. Current (left y-axis) and voltage (right y-axis) during the discharge phase of the test. The markers point out some of the moments in which EIS measurements are performed.

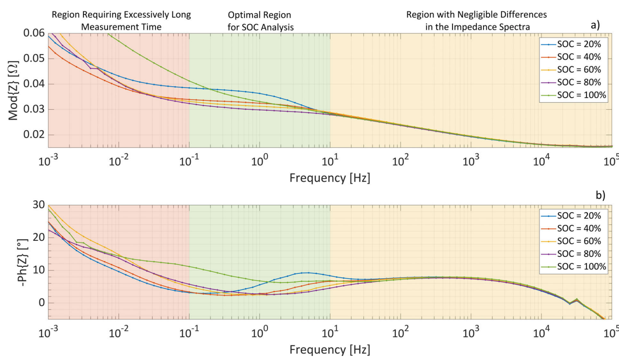

Fig. 3. Bode diagrams of EIS for the DUT measured at different SoC conditions. (a) Magnitude plot. (b) Phase plot.

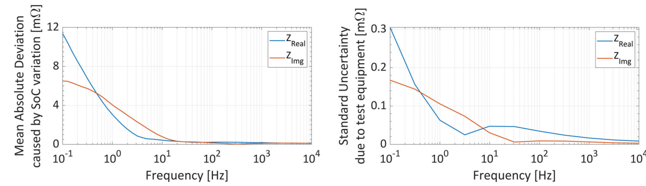

Fig. 4. Comparison between the deviations caused by the SoC variation and the standard uncertainty due to the test equipment.

tests using a climatic chamber. A schematic workflow of the experimental procedure is reported in Table I. The rationale behind the selection of 20 cycles as a duration of the testing campaign is aimed at maintaining the same health condition among the measurements, ensuring consistency across the cycles, and avoiding aging drifts. Battery aging effects can be considered negligible since the cells were charged and discharged using standard slow charge/discharge profiles, as specified by the manufacturer. This is further supported by the observation that no significant deviation in the discharge capacity was detected from the beginning to the end of the experiments. Moreover, visual inspections were performed before and after each test to confirm the structural integrity of both the cell casing and electrodes, ensuring that no external or mechanical degradation occurred during the testing process. Nonetheless, it is worth mentioning that the degradation of the HSC introduces drifts in the impedance values over time that need proper compensating actions, which are beyond the scope of this article.

An illustration of voltage and current during the discharge phase is reported in Fig. 2, with yellow markers pointing out the moment in time at which the EIS measurements are performed (only a few of them are shown for the sake of better readability of the figure).

To select the most suitable frequency setpoints, a preliminary analysis has been conducted, performing EIS measurements in a wide frequency range. The results in terms of Bode diagrams of both the impedance magnitude and phase at different SoC conditions are reported in Fig. 3. To train the proposed algorithm in identifying the SoC from the EIS measurements, it is essential to find a frequency region where the impedance spectra are different under SoC conditions.

As can be seen from Fig. 3, three frequency regions can be identified as follows.

1) The EIS measurements carried out at frequencies higher than 10 Hz highlight only marginal differences under various SoC conditions.
2) Frequency setpoints lower than 100 mHz require excessively long measurement times that cannot be feasible in real applications.
3) The region between 100 mHz and 10 Hz seems to be the optimal tradeoff between measurement duration and variability of the impedance spectra at different SoC conditions.

In Fig. 4, the mean absolute deviations from the real and imaginary components of the impedance generated by SoC variation are compared with the standard measurement uncertainties estimated considering the effects of the test equipment. Fig. 4 allows for further validation of the definition of the selected frequency range [100 mHz, 10 Hz] as the optimal region for evaluating the changes related to SoC variations. Specifically, the deviations in the left plots are referred to the reference impedances measured at SoC = 100%, while the uncertainties are derived from a statistical analysis on 100 EIS consecutive measurements collected at a fixed SoC value of 100%. The plots show that the measurement uncertainty is negligible compared to the absolute deviations, with a maximum value of 0.33 mΩ opposed to deviations of several mΩ caused by SoC variations, proving the validity and robustness of the selected region of investigation.

It is also important to mention that the 0% SoC level is defined as the point at which the knee point in the voltage–capacity characteristic is reached. As a matter of fact, many BMS consider this point as the actual end level of the SoC since the voltage drop after the knee point becomes so rapid that the cell is not capable of correctly fulfilling its supplying role [37].

This choice is mainly justified by the necessity to define a safe and reliable discharge condition that avoids nonlinear regions in voltage–capacity characteristics and irreversible effects on the cell. Overall, for each cycle, the average amount of electric charge stored corresponds to 4.08 Ah.

It is worth noting that all charge and discharge operations were performed using nominal current levels recommended by the manufacturer. As a result, the impedance–SoC relationship is, to some extent, dependent on the specific current profile

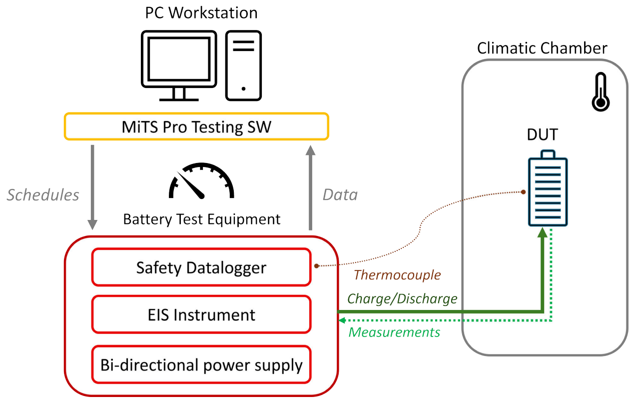

Fig. 5. Schematic representation of the experimental platform.

adopted during the experiments. Since changing the current can alter voltage drops and impedance dynamics, the proposed GPR-based model may produce systematic errors if used outside the trained current level.

However, retraining the network, adding different current ranges, and adapting them to the specific application could address this issue without limiting the applicability of the proposed method.

C. Experimental Platform

In Fig. 5, the measurement setup used for data acquisition is illustrated. The experimental platform used to test the HSC consists of two main instruments: a bidirectional power supply, Arbin LBT 5V-30A, capable of performing charge/discharge cycle schedules up to 16 channels simultaneously, and a Gamry 5000E Interface able to perform EIS measurements in a wide range from 10 μHz to 100 kHz in both potentiostatic and galvanostatic modes. More specifically, the battery tester allows maximum rates of 5 V and 30 A on each channel, and it can achieve sample frequencies up to 100 Hz with a data acquisition resolution of 24 bits for each channel.

The test equipment is interfaced with the MiTS Pro Testing software installed on a PC workstation to manage the testing schedules and store the measurements. In addition, the setup also integrates an external safety datalogger that monitors the overheating of the cell by means of a T-type thermocouple. Consequently, in case of potentially hazardous conditions in the cell, the measurement system can automatically stop the routine and prevent safety issues. To ensure constant environmental conditions, the DUT is placed inside a climatic chamber, which can regulate the temperature in the range from −40 °C to 180 °C and the humidity level from 10% to 95%.

IV. Results and Discussion

The algorithms described in Section II have been applied to the acquired dataset for testing the SoC evaluation capability of the proposed method.

Initially, the GPR model was deployed with all four features, i.e., the modulus, phase, real, and imaginary values of the measured impedance and all six frequencies, i.e., 0.05, 0.1, 0.5, 1, 5, and 10 Hz. The frequencies are spaced with two times factor to maintain a consistent pattern. The data have been divided into a 70:30 split ratio, where 70% account for the training data (i.e., 14 cycles) and the rest 30% (i.e., six cycles) account for the test data. Moreover, to create an unbiased environment, the 70:30 division has been randomized and repeated ten times, creating ten different training/test datasets with which the GPR model was trained, validated, and tested.

TABLE II

(a) RMSE for Tests 1–5. (b) RMSE for Tests 6–10. (c) Average RMSE for Tests 1–10

(a)

Frequency	Test.1	Test.2	Test.3	Test.4	Test.5
0.05Hz	1.51	1.11	1.36	1.24	1.53
0.1Hz	1.36	1.23	1.19	1.19	0.33
0.5Hz	4.20	4.51	3.84	5.10	3.55
1Hz	7.28	7.70	7.62	7.38	7.46
5Hz	14.82	14.84	14.47	28.90	14.4
10Hz	9.68	10.33	9.99	12.24	9.15

(b)

Frequency	Test.6	Test.7	Test.8	Test.9	Test.10
0.05Hz	1.35	1.43	1.19	1.07	1.30
0.1Hz	1.43	1.30	1.06	1.36	1.46
0.5Hz	4.42	4.77	4.57	4.18	4.67
1Hz	8.26	8.17	8.45	7.28	7.73
5Hz	14.09	14.3	14.39	14.82	14.5
10Hz	9.82	8.87	9.22	9.92	9.27

(c)

Frequency	Average RMSE
0.05Hz	1.31
0.1Hz	1.19
0.5Hz	4.38
1Hz	7.73
5Hz	15.96
10Hz	9.85

The training, validation, and tests are performed on a 13th generation Intel[1] Core i9 laptop with MATLAB R2023b. The Bayesian optimization is deployed during training with a maximum of 30 iterations. A first validation of the model has been performed considering a fivefold cross validation.

The RMSEs of the tests performed are summarized in Table II(a)–(c), where the former corresponds to the first five tests, the second one corresponds to the last five tests, and the latter corresponds to the average RMSE value.

As per the results depicted above, a general pattern can be deduced, i.e., with the increase in frequency, the RMSE increases as well. However, anomalies are detected at 0.1 and 10 Hz, where deviant behavior is present in some tests. The RMSE peaks at 5 Hz, and the least RMSE is seen to be present at 0.1 Hz.

To simplify the measurement procedure, only one frequency should be selected, and from the above analysis, it appears that the best candidate is the 0.1-Hz frequency. However,

[1]Registered trademark.

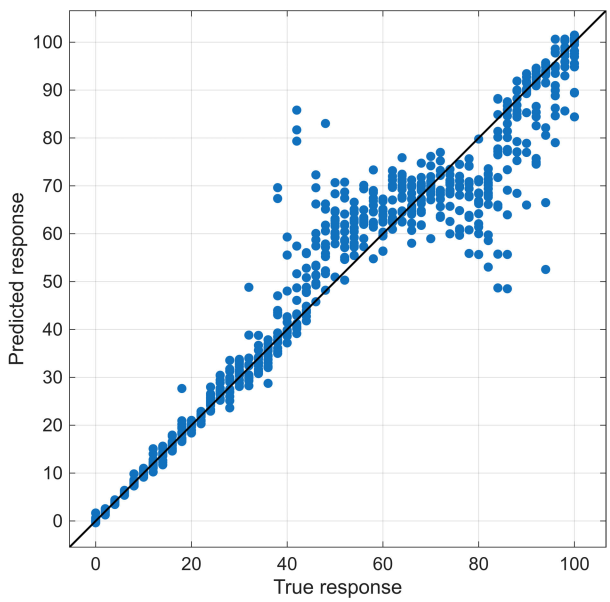

Fig. 6. Comparison of predicted and corrected SoC versus observed SoC (Test 1).

the choice of subhertz frequency intrinsically entails a longer measurement procedure. Among the higher frequencies, the 1 Hz is the one with the best results, although the obtained RMSE is unacceptable in practical applications, even considering a possible postprocessing technique. From a more detailed analysis of the results, it could be observed that while a generally higher RMSE is achieved with higher frequencies, a still good performance is obtained when low SoC values are considered.

In Fig. 6, an example of SoC predicted values versus the true values is reported. In this example, the results from Test 1 are shown. With SoC values lower than 30%, the error between the predicted value and the true value is lower, while more scattered values are present in the higher SoC range.

Hence, to minimize the overall operating time and in turn increase the resource efficiency of the proposed approach, two different frequencies have been selected and applied to the area of the evaluated SoC. For the SoC in the range of [0, 30], the values pertaining to 1 Hz are used to train the GPR model, while in the range of [30, 100], the 0.1-Hz frequency has been used. This choice depends on the fact that generally, the discharge curve of an HSC has a strong nonlinear behavior, with a rapid decrease when the SoC approaches zero. Therefore, when the SoC value is high, a slow change is observed, and it is possible to perform a more scattered evaluation. Instead, in the case of low SoCs, it can be important to perform close evaluations to avoid an unexpected full discharge of the HSC.

Consequently, while low frequencies allow a more accurate estimate and can be used for higher SoC values, even if a longer measurement procedure is involved, higher frequencies can be used when the SoC is low, allowing more frequent measurements and still guaranteeing good accuracy. Moreover, considering that the input features can be divided into two sets {imaginary part, real part} or {magnitude, phase} that

TABLE III
RMSE AND FEATURE SELECTION

Impedance Features	**Freq.**	**SoC Range**	**RMSE**	**RMSE Total**
Real & imaginary	0.1 Hz	[30,100]	1.72	1.50
	1 Hz	[0,30]	0.77	
Modulus & phase	0.1 Hz	[30,100]	1.70	1.48
	1 Hz	[0,30]	0.76	
All features (proposed)	0.1 Hz	[30,100]	1.70	1.48
	1 Hz	[0,30]	0.74	

are strictly correlated with each other, in an actual hardware implementation of the BMS, the input features set could be reduced. In Table III, the results varying the input set of features are presented, considering the average value of RMSE over all ten randomized tests. In Table III, the values for 0.1 Hz correspond to the SoC window of [30, 100], and the values for 1 Hz correspond to the SoC window of [0, 30]. The overall RMSEs for both 0.1 and 1 Hz when the GPR has been applied are calculated according to the following equation:

$$RMSE_{OV} = \sqrt{(RMSE_{030})^2 \times 0.3 + (RMSE_{30100})^2 \times 0.7} \quad (9)$$

where $RMSE_{OV}$ represents the overall RMSE value. $RMSE_{030}$ and $RMSE_{30100}$ represent the RMSE values for the SoC ranges [0, 30] and [30, 100], respectively.

It is worth noting that the resulting RMSE does not change significantly when varying the input feature set. Furthermore, in the context of this article, the fine-tuning of the ML model has little relevance since the aim is to present a possible new simplified approach to have an accurate SoC prediction based on a single point EIS data. Moreover, the actual choice of the input feature could have more relevance in an actual HW implementation of the whole BMS, where other practical aspects can be considered. For this reason, and for the sake of generality, the tests presented in the rest of this article were carried out, including all four features, leaving to a possible future hardware implementation the choice of the final set to be used.

After an exhaustive training and testing session, the results are further improved by performing interpolation and applying an error calibration technique. In particular, the linearization is computed by using the next and the previous predicted value. A threshold is fixed, serving as a measure of whether the interpolated or the predicted value shall be passed forward as the predicted SoC. After linearization, an error calibration is performed by utilizing the first discharge cycle to compute the error variable and correcting the subsequent cycles to remove any systematic error. The results are documented in Table IV.

The final values of RMSE, after the three-point linearization and error calibration, are stated in the last column of Table IV. The minimum value achieved is for the RD #8, which is 0.78, whereas the maximum value is for the RD #9 of 1.15. The final average value of 0.94 shows highly satisfactory results. The comparison of the predicted SoC and the final SoC (after three-point linearization and error calibration) for one of the RDs can be visually seen in Fig. 7. The improvement induced

TABLE IV

RMSE in Both Validation and Test, and After the Postprocessing Algorithm

Randomized Datasets (RD)		GPR RMSE – Frequencies/ SoC Range 0.1 Hz [30,100]	GPR RMSE – Frequencies/ SoC Range 1 Hz [0,30]	Overall GPR RMSE	Post processing RMSE
1	**Val.**	1.57	0.78	1.38	1.15
	Test	1.57	0.83	1.39	
2	**Val.**	1.60	0.81	1.41	0.87
	Test	1.44	0.74	1.27	
3	**Val.**	1.69	0.86	1.49	0.79
	Test	1.37	0.68	1.21	
4	**Val.**	1.77	0.73	1.53	0.79
	Test	1.33	0.91	1.22	
5	**Val.**	1.55	0.66	1.34	1.00
	Test	1.66	1.00	1.49	
6	**Val.**	1.60	0.84	1.41	1.15
	Test	1.67	0.63	1.44	
7	**Val.**	1.56	0.85	1.38	0.82
	Test	1.54	0.63	1.33	
8	**Val.**	1.57	0.80	1.38	0.78
	Test	1.23	0.61	1.08	
9	**Val.**	1.63	0.77	1.42	1.15
	Test	1.57	0.79	1.39	
10	**Val.**	1.54	0.78	1.36	1.07
	Test	1.70	0.74	1.48	
Average RMSE over 10 RDs					**0.94**

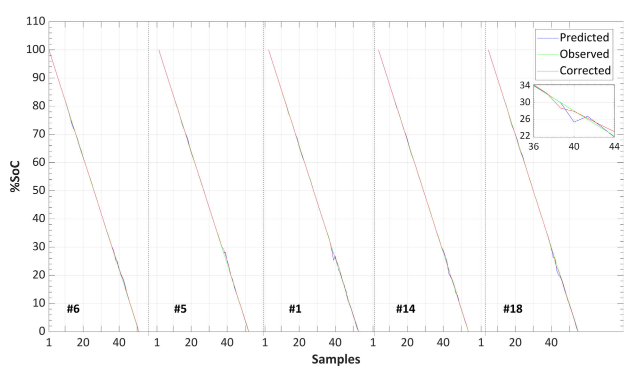

Fig. 7. Comparison of predicted and corrected SoC versus observed SoC. The number in the bottom side refers to the randomized test cycle.

by the postprocessing stage can be viewed in the zoomed-in view version of the graph in Fig. 7. The green line indicates the observed SoC. The blue line indicates the predicted SoC, which clearly struggles to imitate the observed value within the illustrated window. The red line depicts the SoC after the postprocessing phase and hence shows a considerable improvement in comparison with the predicted value.

Fig. 8 presents the pdfs of the absolute SoC error in all the test cases for the raw predicted values (blue trend) and after

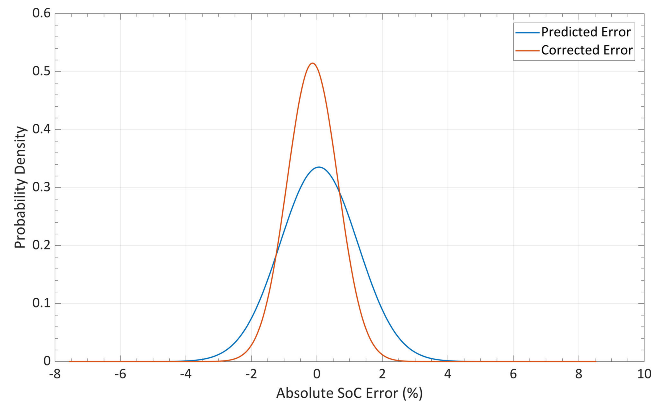

Fig. 8. Probability distribution of predicted and calibrated SoC errors.

calibration (red line). The application of the calibration procedure allows for obtaining a narrower probability distribution with significantly lower standard deviation and a slightly lower mean value compared to the distribution of the absolute SoC error before correction.

This confirms the validity of the calibration algorithm in that the corrected SoC errors are more tightly concentrated around the mean (closer to zero), reflecting higher precision and reduced variance.

On the other hand, the wider spread of the predicted error distribution points toward greater variability in the prediction values. A narrower distribution indicates smaller and more consistent error values, which is desirable in SoC estimation applications where accuracy and reliability are critical. Hence, the corrected/calibrated version demonstrates a statistically improved performance, further validating the error calibration process.

To better demonstrate the feasibility of the approach, the ten randomized trained models were tested using two additional datasets collected on different devices. More specifically, Dataset #N1 has been obtained by testing a new cell of the same manufacturer with the same characteristics and operating conditions as the initial one. Similarly, Dataset #N2 has been obtained on another HSC (still, the same device model and manufacturer) working at a different operating condition (35 °C instead of 20 °C like other datasets), for a total of three identical cells tested (including the original one always used for training).

In Table V, the results of the tests in these different conditions after the GPR model prediction, the interpolation phase, and the calibration phase are presented.

The trained model remained the same as the results presented in Table IV, and no new retraining was performed to demonstrate the generalization capability of the approach. As can be seen, the previous results confirm the feasibility of the proposed approach, with RMSEs comparable to those obtained with the first dataset.

A clear improvement is observed when the postprocessing stage is applied. Indeed, it helps in adapting the ML-trained model to the specific dataset, reducing the impact of testing it on unknown data.

TABLE V
TEST RESULTS OF THE PROPOSED MODEL WITH DIFFERENT CELLS AND DIFFERENT OPERATING CONDITIONS

Dataset	RMSE after GPR	RMSE after Interpolation	RMSE after Calibration
#N1	1.38	1.00	0.90
#N2	1.65	1.21	1.13

TABLE VI
COMPARISON WITH THE STATE-OF-THE-ART

Algorithm	FEATURES	FP	RMSE	FI
OCV	--	--	1.44	--
GPR [38]	Real, Imaginary	14	1.1	15.4
GPR [39]	Real, Imaginary	54	1.46	78.85
GPR [40]	Real, Imaginary	54	0.36	19.44
DNN [40]	Real, Imaginary	54	0.20	10.80
GPR [31]	| |, φ, Real, Imaginary	1	1.56	1.56
Proposed	| |, φ, Real, Imaginary	**1**	**0.99**	**0.99**

For further insight, the results from the proposed framework are compared with state-of-the-art existing literature for the SoC estimation of an ESS. The comparison is performed keeping in view that not much research has been done in the field of EIS and SC collectively; hence, other ESSs along with EIS are also taken into consideration. The results are reported in Table VI.

First, an OCV-based method has been considered as a state-of-the-art comparative methodology in Table VI, while the CC method implemented directly by the battery test equipment using the current measured during the test has been used as a reference SoC value (i.e., ground truth) against which the RMSE has been calculated.

In [38], a Monte Carlo ensemble generated experimental data with EIS and ECM features is used to train a GPR model with an RBF kernel. The minimum RMSE for the EIS feature set is 1.1, with a maximum RMSE of 3.7 for 200 and 20 training samples pertaining to the Monte Carlo ensemble. In [39], a GPR and a linear regression model are proposed to estimate the SoC of the LiB using the parameters acquired through EIS. The tests are conducted using different correlation values and at multiple temperatures. The results present a minimum RMSE of 1.46 for the GPR model at 25 °C. Another article [40] deploys a DNN and a GPR to estimate the SoC with features extracted through EIS. The GPR uses an isotropic exponential kernel, and the features utilized for model training are the real and imaginary parts of the impedance, with a resulting RMSE of 0.36. The DNN has two hidden layers with a mean squared error loss function, resulting in an RMSE of 0.2.

Even though the RMSE reported in [40] is less than the proposed approach, 54 FPs have been used [1 mHz, 6 kHz] for each sample, as opposed to only 1 in the case of the proposed approach. Indeed, according to the expected SoC value, which can be evaluated considering the last computed SoC value, in the proposed approach, only one frequency has to be set in the measurement procedure. A larger number of FPs results in a longer operating time for the EIS procedure and hence makes the approach less suitable for an in situ assessment. Therefore, a feasibility index (FI) has been calculated, which is the product of the RMSE and the number of FPs. This FI indicates the overall feasibility of the cited and the proposed approaches as a compromise between the RMSE and the complexity of the approach. The FI clearly indicates a substantial difference between the proposed and existing approaches. The proposed RMSE in Table VI is computed considering the average value among all the tested datasets. Moreover, from the comparison with the previous research [31], it is also evident that using two different FPs for two different SoC ranges further reduces the FI, making the in situ measurements even more practicable and improving the state-of-the-art in SoC evaluation based on EIS data.

It is important to note that the proposed methodology has been validated under conditions where aging effects are negligible. In HSCs, aging is typically associated with an increase in equivalent series resistance (ESR), a gradual loss of capacitance, and modifications in the shape of the impedance spectrum, particularly in the low- and mid-frequency regions [41], [42]. Such changes may alter the impedance values at the selected FPs and consequently affect the accuracy of the trained regression model. Although aging was intentionally minimized in this study by limiting the experimental campaign to 20 cycles under nonstressful operating conditions, long-term degradation could introduce systematic drifts in the impedance–SoC relationship. In practical applications, these effects could be mitigated through periodic recalibration, retraining of the regression model, or adaptive selection of FPs.

V. CONCLUSION

In this article, an innovative approach for the SoC estimation based on EIS data collected on an HSC is proposed. A GPR algorithm has been trained and tested using the data acquired through EIS, with the modulus, phase, real, and imaginary values of the impedance as features. The data are extracted within a controlled environment, with the HSC as the DUT. A selective approach is presented, applying two different frequencies to two separate SoC ranges, i.e., [0, 30] and [30, 100]. The data related to 0.1 Hz are utilized to train the model for the range [30, 100], and the data related to 1 Hz are used to train the GPR model within the window [0, 30]. While the lower frequency performs well in terms of RMSE, it requires a higher measurement time; collecting data at the higher frequency is much faster, although it generally shows a lower RMSE. Hence, this dual-frequency approach provides the opportunity to optimize the RMSE and the operating time.

A total of 20 discharge cycles is collected and randomized to maintain an unbiased scheme. Within the GPR, the anisotropic kernel is the main entity that captures the similarities among the data points, which is then used to form the relationship for SoC prediction. Subsequently, a linear three-point interpolation and an error calibration using a single discharge cycle are performed. The estimated SoC results in an average RMSE of 1.52 and 0.99, without and with the postprocessing phase, respectively, considering all the tested datasets. When compared with the literature, these values show good performance, especially if the low number of FPs utilized in the proposed approach is considered, demonstrating the feasibility of the approach for in situ measurements.

References

[1] F. Asgarian, S. R. Hejazi, and H. Khosroshahi, "Investigating the impact of government policies to develop sustainable transportation and promote electric cars, considering fossil fuel subsidies elimination: A case of Norway," *Appl. Energy*, vol. 347, Oct. 2023, Art. no. 121434, doi: 10.1016/j.apenergy.2023.121434.

[2] L. Breglio et al., "A model-based strategy for active balancing and SoC and SoH estimations of an automotive battery management system," *Modelling*, vol. 5, no. 3, pp. 911–935, Aug. 2024, doi: 10.3390/modelling5030048.

[3] M. Adaikkappan and N. Sathiyamoorthy, "Modeling, state of charge estimation, and charging of lithium-ion battery in electric vehicle: A review," *Int. J. Energy Res.*, vol. 46, no. 3, pp. 2141–2165, Oct. 2021, doi: 10.1002/er.7339.

[4] R. T. Yadlapalli, R. R. Alla, R. Kandipati, and A. Kotapati, "Super capacitors for energy storage: Progress, applications and challenges," *J. Energy Storage*, vol. 49, May 2022, Art. no. 104194, doi: 10.1016/j.est.2022.104194.

[5] A. G. Olabi, Q. Abbas, A. Al Makky, and M. A. Abdelkareem, "Supercapacitors as next generation energy storage devices: Properties and applications," *Energy*, vol. 248, Jun. 2022, Art. no. 123617, doi: 10.1016/j.energy.2022.123617.

[6] O. A. AlKawak, J. R. R. Kumar, S. S. Daniel, and C. V. K. Reddy, "Hybrid method based energy management of electric vehicles using battery-super capacitor energy storage," *J. Energy Storage*, vol. 77, Jan. 2024, Art. no. 109835, doi: 10.1016/j.est.2023.109835.

[7] K. Subasinghage, K. Gunawardane, N. Padmawansa, N. Kularatna, and M. Moradian, "Modern supercapacitors technologies and their applicability in mature electrical engineering applications," *Energies*, vol. 15, no. 20, p. 7752, Oct. 2022, doi: 10.3390/en15207752.

[8] J. Rivera-Barrera, N. Muñoz-Galeano, and H. Sarmiento-Maldonado, "SoC estimation for lithium-ion batteries: Review and future challenges," *Electronics*, vol. 6, no. 4, p. 102, Nov. 2017, doi: 10.3390/electronics6040102.

[9] V. Chandran, C. K. Patil, A. Karthick, D. Ganeshaperumal, R. Rahim, and A. Ghosh, "State of charge estimation of lithium-ion battery for electric vehicles using machine learning algorithms," *World Electr. Vehicle J.*, vol. 12, no. 1, p. 38, Mar. 2021, doi: 10.3390/wevj12010038.

[10] S. Guo and L. Ma, "A comparative study of different deep learning algorithms for lithium-ion batteries on state-of-charge estimation," *Energy*, vol. 263, Jan. 2023, Art. no. 125872, doi: 10.1016/j.energy.2022.125872.

[11] S. Ali, M. Stighezza, G. Chiorboli, I. De Munari, and V. Bianchi, "An optimized long short term memory and Gaussian process regression based framework for state of charge estimation," in *Proc. IEEE Int. Workshop Metrol. Automot. (MetroAutomotive)*, Bologna, Italy, Jun. 2024, pp. 94–99, doi: 10.1109/MetroAutomotive61329.2024.10615514.

[12] E. Chemali, P. J. Kollmeyer, M. Preindl, and A. Emadi, "State-of-charge estimation of Li-ion batteries using deep neural networks: A machine learning approach," *J. Power Sources*, vol. 400, pp. 242–255, Oct. 2018, doi: 10.1016/j.jpowsour.2018.06.104.

[13] S. Wang, M. Jiao, R. Zhou, Y. Ren, H. Liu, and C. Lian, "A multi-dimensional machine learning framework for accurate and efficient battery state of charge estimation," *J. Power Sources*, vol. 623, Dec. 2024, Art. no. 235417, doi: 10.1016/j.jpowsour.2024.235417.

[14] J. Wang, "An intuitive tutorial to Gaussian process regression," *Comput. Sci. Eng.*, vol. 25, no. 4, pp. 1–8, Jul. 2023, doi: 10.1109/mcse.2023.3342149.

[15] O. Ali et al., "On-line WSN SoC estimation using Gaussian process regression: An adaptive machine learning approach," *Alexandria Eng. J.*, vol. 61, no. 12, pp. 9831–9848, Dec. 2022, doi: 10.1016/j.aej.2022.02.067.

[16] F. Xiao, C. Li, Y. Fan, G. Yang, and X. Tang, "State of charge estimation for lithium-ion battery based on Gaussian process regression with deep recurrent kernel," *Int. J. Electr. Power Energy Syst.*, vol. 124, Jan. 2021, Art. no. 106369, doi: 10.1016/j.ijepes.2020.106369.

[17] B. Zazoum, "Lithium-ion battery state of charge prediction based on machine learning approach," *Energy Rep.*, vol. 9, pp. 1152–1158, Mar. 2023, doi: 10.1016/j.egyr.2023.03.091.

[18] P. Dhal and C. Azad, "A comprehensive survey on feature selection in the various fields of machine learning," *Int. J. Speech Technol.*, vol. 52, no. 4, pp. 4543–4581, Jul. 2021, doi: 10.1007/s10489-021-02550-9.

[19] W. Zhou, Y. Zheng, Z. Pan, and Q. Lu, "Review on the battery model and SOC estimation method," *Processes*, vol. 9, no. 9, p. 1685, Sep. 2021, doi: 10.3390/pr9091685.

[20] M. Zhang et al., "Electrochemical impedance spectroscopy: A new chapter in the fast and accurate estimation of the state of health for lithium-ion batteries," *Energies*, vol. 16, no. 4, p. 1599, Feb. 2023, doi: 10.3390/en16041599.

[21] Y. Liu, L. Wang, D. Li, and K. Wang, "State-of-health estimation of lithium-ion batteries based on electrochemical impedance spectroscopy: A review," *Protection Control Mod. Power Syst.*, vol. 8, no. 1, pp. 1–17, Aug. 2023, doi: 10.1186/s41601-023-00314-w.

[22] E. Buchicchio, A. De Angelis, F. Santoni, P. Carbone, F. Bianconi, and F. Smeraldi, "Battery SOC estimation from EIS data based on machine learning and equivalent circuit model," *Energy*, vol. 283, Nov. 2023, Art. no. 128461, doi: 10.1016/j.energy.2023.128461.

[23] M. Messing, T. Shoa, R. Ahmed, and S. Habibi, "Battery SoC estimation from EIS using neural nets," in *Proc. IEEE Transp. Electrific. Conf. Expo (ITEC)*, Jun. 2020, pp. 588–593, doi: 10.1109/ITEC48692.2020.9161523.

[24] X. Zhang et al., "SOC estimation of lithium-ion batteries using equivalent circuit model and Nyquist plots from EIS data: A machine learning approach," *J. Electroanal. Chem.*, vol. 987, Jun. 2025, Art. no. 119093, doi: 10.1016/j.jelechem.2025.119093.

[25] B. Jiang, J. Zhu, X. Wang, X. Wei, W. Shang, and H. Dai, "A comparative study of different features extracted from electrochemical impedance spectroscopy in state of health estimation for lithium-ion batteries," *Appl. Energy*, vol. 322, Sep. 2022, Art. no. 119502, doi: 10.1016/j.apenergy.2022.119502.

[26] Z. Wang, G. Feng, D. Zhen, F. Gu, and A. Ball, "A review on online state of charge and state of health estimation for lithium-ion batteries in electric vehicles," *Energy Rep.*, vol. 7, pp. 5141–5161, Nov. 2021, doi: 10.1016/j.egyr.2021.08.113.

[27] D. Lemian and F. Bode, "Battery-supercapacitor energy storage systems for electrical vehicles: A review," *Energies*, vol. 15, no. 15, p. 5683, Aug. 2022, doi: 10.3390/en15155683.

[28] Q. Deng, D. Qiu, Z. Xie, B. Zhang, and Y. Chen, "Online SOC estimation of supercapacitor energy storage system based on fractional-order model," *IEEE Trans. Instrum. Meas.*, vol. 72, pp. 1–10, 2023, doi: 10.1109/TIM.2023.3280524.

[29] K. Wang et al., "State of charge estimation of composite energy storage systems with supercapacitors and lithium batteries," *Complexity*, vol. 2021, no. 1, pp. 1–15, Feb. 2021, doi: 10.1155/2021/8816250.

[30] Y. Xu et al., "State of charge estimation of supercapacitors based on multi-innovation unscented Kalman filter under a wide temperature range," *Int. J. Energy Res.*, vol. 46, no. 12, pp. 16716–16735, Jul. 2022, doi: 10.1002/er.8334.

[31] V. Bianchi, F. Canzanella, S. Ali, I. De Munari, L. Ciani, and G. Patrizi, "A single-point EIS measurement for SOC estimation of supercapacitor," in *Proc. IEEE Int. Instrum. Meas. Technol. Conf. (I2MTC)*, Chemnitz, Germany, May 2025, pp. 1–6.

[32] J. Pedro Aguiar dos Santos et al., "Best practices for electrochemical characterization of supercapacitors," *J. Energy Chem.*, vol. 80, pp. 265–283, May 2023, doi: 10.1016/j.jechem.2022.12.034.

[33] M. M. Noack, H. Luo, and M. D. Risser, "A unifying perspective on non-stationary kernels for deeper Gaussian processes," *APL Mach. Learn.*, vol. 2, no. 1, Feb. 2024, doi: 10.1063/5.0176963.

[34] M. M. Noack and J. A. Sethian, "Advanced stationary and nonstationary kernel designs for domain-aware Gaussian processes," *Commun. Appl. Math. Comput. Sci.*, vol. 17, no. 1, pp. 131–156, Oct. 2022, doi: 10.2140/camcos.2022.17.131.

[35] *Datasheet: '4.2V4000F' Rechargeable Nano-Pouch Capacitor's Datasheet*, GongHe Electronics, REV: A2.0, Guangdong, China, Dec. 2022.

[36] G. Patrizi, F. Canzanella, A. Bartolini, and L. Ciani, "Influence of relaxation time on electrochemical impedance spectroscopy measurements in electric vehicle charger," in *Proc. IEEE Int. Instrum. Meas. Technol. Conf. (I2MTC)*, Chemnitz, Germany, May 2025, pp. 1–6, doi: 10.1109/I2MTC62753.2025.11078970.

[37] L. Schärtel, B. Reick, M. Pfeil, and R. Stetter, "Analysis and synthesis of architectures for automotive battery management systems," *Appl. Sci.*, vol. 12, no. 21, p. 10756, Oct. 2022, doi: 10.3390/app122110756.

[38] F. Santoni, A. De Angelis, A. Moschitta, and P. Carbone, "Training Gaussian process regression through data augmentation for battery SOC estimation," *J. Energy Storage*, vol. 98, Sep. 2024, Art. no. 113073, doi: 10.1016/j.est.2024.113073.

[39] I. Babaeiyazdi, A. Rezaei-Zare, and S. Shokrzadeh, "State of charge prediction of EV Li-ion batteries using EIS: A machine learning approach," *Energy*, vol. 223, May 2021, Art. no. 120116, doi: 10.1016/j.energy.2021.120116.

[40] Y. Li, M. Maleki, S. Banitaan, and M. Chen, "Data-driven state of charge estimation of Li-ion batteries using supervised machine learning methods," in *Proc. 20th IEEE Int. Conf. Mach. Learn. Appl. (ICMLA)*, Dec. 2021, pp. 873–878, doi: 10.1109/ICMLA52953.2021.00144.

[41] G. Patrizi et al., "Study of accelerated aging effects on hybrid supercapacitors under different fast-charging strategies," *IEEE Trans. Instrum. Meas.*, vol. 74, pp. 1–15, 2025, doi: 10.1109/TIM.2025.3577838.

[42] N. El Ghossein, A. Sari, and P. Venet, "Lifetime prediction of lithium-ion capacitors based on accelerated aging tests," *Batteries*, vol. 5, no. 1, p. 28, Mar. 2019, doi: 10.3390/batteries5010028.

Gabriele Patrizi (Member, IEEE) received the master's degree (cum laude) in electronic engineering and the Ph.D. degree in industrial and reliability engineering from the University of Florence, Florence, Italy, in 2018 and 2022, respectively.

In 2022, he joined the Institute of Electronic Packaging Technology (IAVT), Dresden Technical University, Dresden, Germany, as a Visiting Post-Doctoral Researcher. Currently, he is an Assistant Professor with the Department of Information Engineering, University of Florence. His research interests include lifecycle reliability, condition monitoring for fault diagnosis, data-driven prognostics and health management, and instrumentation and measurement for reliability analysis.

Dr. Patrizi was a recipient of the 2023 IEEE IMS Best Dissertation Award and the 2025 IEEE IMS Outstanding Young Engineer Award for his contributions to the advancement of I&M Methods in Diagnostic, Prognostic and Health Management. He is the Associate Editor-in-Chief of IEEE Transactions on Instrumentation and Measurement (TIM).

Sadia Ali (Member, IEEE) received the bachelor's degree in electrical engineering from the University of Engineering and Technology, Lahore, Pakistan, in 2013, and the master's degree in electrical engineering from Comsats University, Islamabad, Pakistan, in 2018, with specialization in automation and control systems. She is currently pursuing the Ph.D. degree in automotive engineering for intelligent mobility with the University of Parma, Parma, Italy, and the University of Bologna, Bologna, Italy.

She has over nine years of experience as a Laboratory Engineer at the Department of Electrical and Computer Engineering, International Islamic University, Islamabad. She has a number of conference and journal publications. Her research interests include electric vehicles, intelligent mobility, electrical machinery, automation, and control systems.

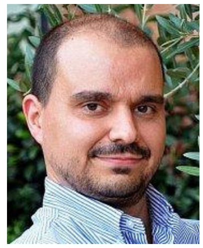

Lorenzo Ciani (Senior Member, IEEE) received the M.S. degree in electronic engineering and the Ph.D. degree in industrial and reliability engineering from the University of Florence, Florence, Italy, in 2005 and 2009, respectively.

He is currently a Full Professor with the Department of Information Engineering, University of Florence. He has authored or co-authored more than 200 peer-reviewed journal articles and conference papers. His current research interests include system reliability, availability, maintainability, safety, reliability evaluation test, and analysis for electronic systems and devices, fault detection and diagnosis, and electrical and electronic instrumentation and measurement.

Prof. Ciani is a member of the IEEE IMS TC-32 Fault Tolerant Measurement Systems. He received the 2015 IEEE I&M Outstanding Young Engineer Award for his contribution to the advancement of instrumentation and measurement in the field of reliability analysis. He is a Senior Area Editor of IEEE Transactions on Instrumentation and Measurement and an Associate Editor of IEEE Access.

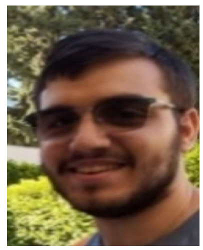

Fabio Canzanella (Member, IEEE) received the B.S. degree in electronic and telecommunications engineering and the M.S. degree in electronic engineering from the University of Florence, Florence, Italy, in 2020 and 2023, respectively, where he is currently pursuing the Ph.D. degree in smart industry.

His research activities center on the electrical and lifecycle characterization of energy storage devices, with a particular focus on the development of methodologies to estimate the state-of-health (SOH) and predict the remaining useful life (RUL).

Ilaria De Munari (Senior Member, IEEE) received the M.Sc. degree in electronic engineering and the Ph.D. degree in information technologies from the University of Parma, Parma, Italy, in 1991 and 1995, respectively.

In 1997, she joined the Department of Information Engineering (now Department of Engineering and Architecture), University of Parma, as an Assistant Researcher, and then as an Associate Professor of electronics, and since 2024, she has been a Full Professor. She has authored or co-authored more than 100 papers in technical journals or proceedings of international conferences. Her past research interests include the reliability of electronic devices and the design of electronic systems for active assisted living. In this framework, she was involved in several European projects. Her current research interests include the design of digital systems based on microcontrollers and field-programmable gate arrays (FPGAs). In particular, she is dealing with the design of sensors for human activity recognition, electrochemical applications, and the evaluation of the battery state-of-charge through machine learning algorithms; moreover, she dealt with the FPGA implementation of arithmetic circuits and error correction code techniques.

Dr. Munari is an Associate Editor of IEEE Access.

Valentina Bianchi (Senior Member, IEEE) received the B.Sc. and M.Sc. degrees in electronic engineering and the Ph.D. degree from the Department of Information Engineering, University of Parma, Parma, Italy, in 2003, 2006, and 2010, respectively.

She is currently an Associate Professor with the Department of Information Engineering, University of Parma. She has participated in several national and international projects. She has authored or co-authored over 50 papers in international journals or proceedings of conferences. Her current research interests include the design and validation of sensors for human activity recognition and for electrochemical and agrifood applications. Moreover, she is involved in designing digital systems implemented on field-programmable gate arrays (FPGAs), with a special focus on the design of hardware for machine learning algorithms and arithmetic circuits.

Prof. Bianchi is the Associate Editor-in-Chief of IEEE Transactions on Instrumentation and Measurement.

Open Access funding provided by 'Università degli Studi di Firenze' within the CRUI CARE Agreement